Reduced-order modelling of thermoacoustic instabilities in can-annular combustors

Alessandro Orchini [a], Tiemo Pedergnana [b], Philip E. Buschmann [c], Jonas P. Moeck [c,*], Nicolas Noiray [b]

[a] *Institute of Fluid Dynamics and Technical Acoustics, TU Berlin, Germany*
[b] *CAPS Laboratory, Department of Mechanical and Process Engineering, ETH Zürich, Switzerland*
[c] *Department of Energy and Process Engineering, NTNU Trondheim, Norway*

A R T I C L E   I N F O

A B S T R A C T

Thermoacoustic instabilities in stationary gas turbines may cause high-amplitude limit cycles, leading to damaged components and costly down-time. To better understand the physical origin of such instabilities in a can-annular combustor configuration, we study the properties of the spectrum of a reduced-order can-annular thermoacoustic system. Increased focus is placed on representing the aeroacoustic interaction between the longitudinal eigenmodes of the individual cans with physically relevant models. To represent the acoustic pressure dynamics in the combustor, we combine an analytical, experimentally validated model for the can-to-can impedance with a frequency-dependent model of the flame response in the cans to acoustic perturbations. By using this approach, we perform a parametric study of the linear stability of an atmospheric can-annular thermoacoustic system, and emphasize general features of the structure and properties of the eigenvalues and the eigenvectors of can-annular combustors. Lastly, we emphasize the differences in the can-to-can coupling that arise when considering open-end boundary conditions – representative of atmospheric set-ups – or closed-end boundary conditions – representative of real gas turbine combustors.

1. Introduction

1.1. Thermoacoustic instabilities in can-annular combustors

Thermoacoustic instabilities can arise from the constructive interaction of a flame with the sound field in an enclosed volume, such as the combustion chamber of a gas turbine. This classic physical phenomenon was first studied in modern terms by [1]. Insufficiently damped instabilities lead to high-amplitude pressure oscillations in the chamber. These oscillations in turn induce high-cycle fatigue in the metal parts surrounding the enclosure, for instance the turbine vanes, which causes down-time and incurs fees and repair costs for the manufacturer. The modelling, prediction and suppression of thermoacoustic instabilities has come to renewed importance in the last 40 years due to strict emission limits and the resulting increased demand for lean-premixed combustion. In modern combustors for power generation, most of the air flow passes through the burner to ensure a lean mixture. The absence of dilution holes that are commonly found in aeroengines – and that are highly efficient sound absorbers – leads to combustion instability problems similar to those encountered in rocket engines, with the difference that the life span of stationary gas turbines is expected to be in the order of tens of thousands of hours [2].

---

* Corresponding author.
    E-mail address: jonas.moeck@ntnu.no (J.P. Moeck).

Nomenclature

Latin symbols

|	
A_r	Ratio between aperture (A_g) and can (A_c) surface area
b	Bloch number
c_i	Speed of sound
f_i, g_i	Riemann invariants
G	Flame front level set ($G=0$)
K_R	Rayleigh conductivity
L_f	Flame length
l_g	Aperture length
M_x	Mach number
N	Number of cans
p	Pressure
q	Heat release rate
r_{can}	Can radius
R_i	Reflection coefficient
s	Laplace variable
s_L	Flame speed
T	Temperature
u	Velocity
$\bar{u}_c$	Convective velocity in the flame
U_c	Convective velocity in the aperture
Z_i	Impedance

Greek symbols

ω	Angular frequency
ρ	Density
σ	Growth rate
τ	Time delay
ζ	Can-to-can impedance

Other symbols

$\hat{\ }$	Laplace domain variable
$\bar{\ }$	Mean value
$\tilde{\ }$	Non-dimensional impedance (scaled with ρc)
FTF	Flame Transfer Function

Much research has been devoted in the last decade to modelling and understanding thermoacoustics of single-can [3–5] and annular combustion chambers [6,7]. In contrast, modern high-efficiency H-class gas turbines exclusively feature can-annular combustor architectures. In this design, combustion takes place in a number (typically 12 or 16) of cans. The annular turbine inlet, located downstream of the cans, is common to all cans and allows for acoustic cross-talk between neighbouring elements. Upstream coupling via a plenum is also possible, but it will not be considered in this study. The increasing interest in the subject of thermoacoustic instabilities in can-annular combustor architectures is exemplified by numerical and experimental studies performed in academia and in industry, including Siemens [8–11], General Electric [12–14], and Ansaldo Energia Switzerland [15,16].

In the present work, we describe a general reduced-order model for predicting thermoacoustic instabilities in can-annular combustors (Sections 2 and 3). This model is used to study a lab-scale can-annular combustor (Section 4), with the objective of understanding the influence that various physical parameters – viz., the mean flow speed and the magnitude of the heat release rate response – have on the frequency spectrum of the system. The physical counterpart of the modelled setup is located at NTNU, Norway [17]. This experimental setup is a modified version of the one described in [18], with the major difference that the annular combustion chamber has been replaced by a periodic set of weakly coupled ducts. This lab-scale combustor operates at atmospheric conditions, and the cans are (acoustically) open at the downstream end. This is in contrast to the acoustic boundary condition in real gas turbines, in which the flow at the outlet of the cans, in other words, at the turbine inlet, is nearly choked. As discussed in [19], the reflection of acoustic waves at a choked end can be approximated reasonably well by a closed-end boundary condition
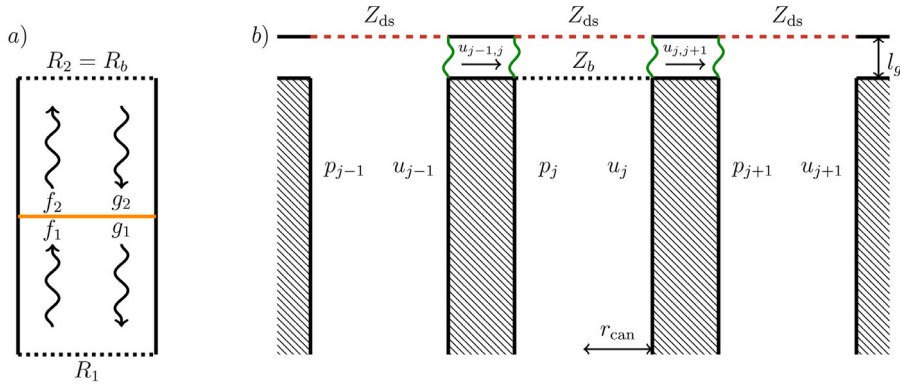
Fig. 1. (*a*) Single-can schematic, highlighting the jump in the acoustics across the flame (in orange) due to temperature and/or area changes. At the downstream end, an effective reflection coefficient R_b is used to obtain a single-can model equivalent to a can-annular system, sketched in (*b*). The cans communicate downstream through apertures having axial extension l_g. Acoustic waves at the downstream end of the cans are partly reflected back in the can by a downstream impedance Z_{ds} (dashed red lines) and partly transmitted to neighbouring cans, via transverse acoustic velocity fluctuations in the apertures. This coupling mechanism is driven by the dynamics of the shear layer that forms at the interface between the cans and the apertures (in green). The effective impedance Z_b, related to R_b via Eq. (8), embeds the reflection of the acoustic waves due to Z_{ds} as well as their transmission through the apertures, as a function of the Bloch wavenumber b. (For interpretation of the references to colour in this figure legend, the reader is referred to the web version of this article.)

— provided that the Mach number upstream of the choked end is small. To address this key difference, in Section 5 we discuss the effect of the downstream boundary condition on the can-to-can coupling and the thermoacoustic spectrum.

1.2. Modelling of the aeroacoustic can-to-can coupling

In this work, special focus is placed on the effect that the can-to-can impedance has on the acoustic pressure dynamics in the chamber. The can-to-can impedance describes the aeroacoustic response at the apertures connecting the ducts. It depends on the interaction between the acoustic pressure fields in neighbouring cans and the aerodynamic modes of the turbulent wake in the apertures connecting them. This acoustic–aerodynamic interaction plays an important role in self-sustained cavity oscillations, a classic physical phenomenon first described by [20]. The model we use is based on impedance measurements of a side-branch aperture presented in Fig. 6(a) of [21], which show a non-trivial behaviour around a frequency corresponding to the least stable aerodynamic mode of the shear layer. For small enough acoustic pressure amplitudes, it was found that the aeroacoustic response of the aperture can be amplifying, which manifests itself in a reflection coefficient magnitude $|R|$ exceeding 1. As the amplitude is increased, the response saturates, an effect that was recently studied numerically using large-eddy simulations (LES) by [22]. These measurements were used in [23] to calibrate an explicit, analytical model able to quantitatively predict the effect of the mean flow speed and the acoustic pressure amplitude on the acoustic impedance over the relevant frequency range.

2. Reduced-order thermoacoustic model

Analogous to [15,24,25], we consider an array of N cans that communicate acoustically at the downstream end via small apertures. The generic configuration that highlights the can-to-can communication is shown in Fig. 1. In this section we present the components of the proposed reduced-order approach, which can be used to model a general can-annular combustor system. The reduced-order model will be applied to an atmospheric can-annular setup, whose details are outlined in [17], to study its thermoacoustic response and the sensitivity of its spectrum.

2.1. Single-can acoustic network model

For the range of frequencies that will be considered in this study, transverse acoustic modes in a can are cut-off. It is thus appropriate to assume planar wave propagation in the axial direction for the acoustics. This is consistent with the results of [15], in which it was shown that non-axial acoustic propagation is relevant only in the vicinity of the connection apertures. To account for these near field effects, the acoustic transmission at the apertures will be modelled by means of an experimentally fitted impedance, presented in Section 3.

The one-dimensional acoustic field is described in terms of its Riemann invariants [26]. By denoting the Riemann invariants travelling downstream and upstream with f and g, respectively, and by considering of the flame (and burner) as a scattering element (see Fig. 1a), the equations for the conservation of mass, momentum and energy yield [27,28]

$$\begin{bmatrix} \hat{g}_1 \\ \hat{f}_2 \end{bmatrix} = \begin{bmatrix} S_{11} & S_{12} \\ S_{21} & S_{22} \end{bmatrix} \begin{bmatrix} \hat{f}_1 \\ \hat{g}_2 \end{bmatrix} + \begin{bmatrix} H_1 \\ H_2 \end{bmatrix} \hat{q}. \tag{1}$$

The subscripts $_1$ and $_2$ denote the region upstream and downstream the flame, respectively, $\hat{q}$ is the unsteady heat release rate response, S_{ij} the elements of the scattering matrix, and H_j constant factors scaling the heat release response to acoustic fluctuations. The specific expressions for S_{ij} and H_j are configuration dependent – e.g., they vary if a mean flow and/or an area change are considered. Their expressions for analytically tractable cases, as the one that will be considered in Section 4, can be found, e.g., in [27,29]. If the response of a burner is included, the scattering matrix cannot be determined analytically, but can be measured experimentally and its elements are generally frequency-dependent expressions [30]. Closure for the acoustics is provided by expressions for the reflection coefficients at the upstream (R_1) and downstream (R_2) boundaries

$$\hat{f}_1 = R_1 e^{-s\tau_1} \hat{g}_1, \quad \hat{g}_2 = R_2 e^{-s\tau_2} \hat{f}_2, \tag{2}$$

with $\tau_j \equiv 2l_j c_j/(c_j^2 - \bar{u}_j^2)$ and $s \equiv \sigma + i\omega$. By substituting these expressions in the conservation laws (1) one obtains

$$\underbrace{\left(\mathcal{I} - \begin{bmatrix} S_{11}R_1 e^{-s\tau_1} & S_{12}R_2 e^{-s\tau_2} \\ S_{21}R_1 e^{-s\tau_1} & S_{22}R_2 e^{-s\tau_2} \end{bmatrix} \right)}_{\mathcal{M}_{ac}} \begin{bmatrix} \hat{g}_1 \\ \hat{f}_2 \end{bmatrix} = \begin{bmatrix} H_1 \\ H_2 \end{bmatrix} \hat{q}, \tag{3}$$

where $\mathcal{I}$ is the identity matrix. In the absence of an unsteady heat release input, $\hat{q} = 0$, the eigenvalues s of the matrix $\mathcal{M}_{ac}$ yield the acoustic eigenvalues.

To account for the effect of the flame on the thermoacoustic stability, the heat release rate term is modelled by means of a Flame Transfer Function (FTF)

$$\hat{q} = \frac{\overline{Q}}{\bar{u}_1} \text{FTF}(s)\hat{u}_1 = \frac{\overline{Q}}{\rho_1 c_1 \bar{u}_1} \text{FTF}(s) \left(\hat{f}_1 - \hat{g}_1 \right) = \left[\frac{\overline{Q}}{\rho_1 c_1 \bar{u}_1} \text{FTF}(s) \left(R_1 e^{-s\tau_1} - 1 \right), 0 \right] \begin{bmatrix} \hat{g}_1 \\ \hat{f}_2 \end{bmatrix}. \tag{4}$$

By defining the matrix

$$\mathcal{M}_{hr} \equiv \begin{bmatrix} H_1 \\ H_2 \end{bmatrix} \left[\frac{\overline{Q}}{\rho_1 c_1 \bar{u}_1} \text{FTF}(s) \left(R_1 e^{-s\tau_1} - 1 \right), 0 \right] \tag{5}$$

the thermoacoustic eigenvalue problem reads

$$\left(\mathcal{M}_{ac}(s) - \mathcal{M}_{hr}(s) \right) \begin{bmatrix} \hat{g}_1 \\ \hat{f}_2 \end{bmatrix} = \begin{bmatrix} 0 \\ 0 \end{bmatrix}. \tag{6}$$

2.2. Bloch boundary conditions

Expressions for the boundary conditions are required to close the thermoacoustic equations. In particular, at the downstream boundary we wish to model the can-to-can acoustic interaction. To understand the effect that can-to-can communication has on the (thermo)acoustic response, it is convenient to make use of Bloch-wave theory [31]. Bloch-wave theory exploits the discrete rotational symmetry of the configuration to reduce the analysis to a sector, in this context referred to as a unit cell, that repeats periodically in space. For a can-annular configuration, this allows to reduce the number of degrees of freedom by a factor N, the number of cans, by representing the acoustic pressure – and analogously all other variables of interest – in terms of Bloch-waves. The Bloch-waves have the form [32]

$$p_b(\theta) = e^{ib\theta} \psi_b(\theta), \tag{7}$$

where ψ_b is a periodic function with period $2\pi/N$, and b is an integer, known as the Bloch wavenumber, that takes values in the range $b \in \{0, \ldots, N-1\}$.

By assuming that all cans are identical, an effective expression for a Bloch-wavenumber-dependent impedance, Z_b, can be derived, allowing to reduce the analysis of the full can-annular system to the analysis of an equivalent single-can system. By referring to Fig. 1b, this effective impedance relates pressure and velocity downstream of a single can, but upstream of its apertures. From the results of [25], this effective can-to-can reflection coefficient R_b can be expressed as

$$R_b = \frac{Z_b - \bar{\rho}c}{Z_b + \bar{\rho}c} = 1 - 2\frac{4\frac{A_r}{\bar{\zeta}}\sin^2\left(\frac{\pi b}{N}\right)}{1 + 4\frac{A_r}{\bar{\zeta}}\sin^2\left(\frac{\pi b}{N}\right)}, \tag{8}$$

where $\bar{\rho}c$ is the characteristic specific acoustic impedance, N the number of cans, b the Bloch wavenumber, A_r the ratio between the cross section of the can-to-can aperture and the cross section of the can[1], and $\bar{\zeta}$ the (non-dimensional) impedance that links the acoustic pressure difference between two adjacent cans and the acoustic velocity:

$$\bar{\zeta} \equiv \frac{\zeta}{\bar{\rho}c} = \frac{1}{\bar{\rho}c} \frac{\hat{p}_j - \hat{p}_{j+1}}{\hat{u}_{j,j+1}}. \tag{9}$$

---

[1] These are the areas of the green and red surfaces in Fig. 6, respectively.
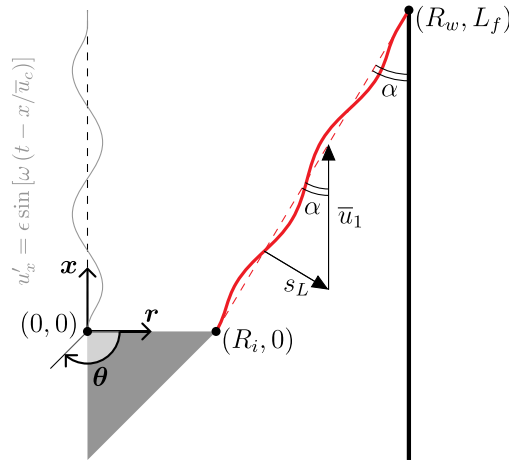
Fig. 2. Geometry of the axisymmetric V-flame dynamics modelled with the *G*-equation. The steady flame (red dashed line) forms an angle α with the can wall, determined by the flame speed s_L and the axial mean flow velocity $\overline{u}_1$. An axially travelling perturbation, u'_x, induces oscillations in the flame front (thick red line), which in turn cause heat release rate fluctuations, quantified by the FTF (14). (For interpretation of the references to colour in this figure legend, the reader is referred to the web version of this article.)

In [25] a simple purely reactive can-to-can impedance model was used. In this study we shall instead adopt a more realistic empirical model, containing both a reactive term and a resistive term, fitted to experimental data, as discussed in Section 3.

Eq. (8) has, however, been derived with some restrictions, specifically that (i) the Helmholtz number defined by He $\equiv (sl_g)/c$, where l_g is the axial extension of the aperture, is negligible; (ii) the cans are acoustically closed after the apertures, thus having $Z_{ds} = \infty$; (iii) the mean flow effects due to a non-zero Mach number grazing flow along the aperture are negligible. Although assumption (i) holds in most practical cases, the same is not true for the others. It was in fact shown in [33] that the effect of the mean flow is non-negligible already for moderate Mach numbers. Moreover, a downstream closed boundary condition does not represent the correct physics for atmospheric test-rigs, which normally have open ends. Assumptions (ii) and (iii) can be relaxed, and a more general expression for the effective reflection coefficient can be derived, which retains the Mach number effects and an arbitrary downstream impedance. It reads [34]

$$R_b = 1 - 2 \frac{\left(1 - \mathrm{M}_x^2\right) + 4A_r/\tilde{\zeta}(\mathrm{M}_x + \tilde{Z}_{ds}) \sin^2\left(\frac{\pi b}{N}\right)}{\left(\tilde{Z}_{ds} + 1\right)\left(1 - \mathrm{M}_x^2\right) + 4A_r/\tilde{\zeta}(\mathrm{M}_x + \tilde{Z}_{ds}) \sin^2\left(\frac{\pi b}{N}\right)}, \tag{10}$$

where we have introduced the (axial) Mach number $\mathrm{M}_x = \overline{u}_2/c_2$. It can be verified that, in the zero Mach number and infinite downstream impedance case, Eq. (8) is retrieved.

At the downstream end of our reduced-order can model we shall therefore set $R_2 = R_b$, which makes the thermoacoustic problem (6) Bloch-number dependent.

2.3. Flame transfer function

The unsteady heat release rate response is chosen to be that of an axisymmetric, laminar V-flame. The flame dynamics is modelled via the kinematic *G*-equation, which tracks the flame front – assumed to be infinitely thin – as the level set $G = 0$, and reads

$$\frac{\partial G}{\partial t} + \boldsymbol{u} \cdot \nabla G = s_L |\nabla G|. \tag{11}$$

Although simplistic, this model captures the general characteristics of a flame transfer function well, as discussed in Section 4.

The underlying velocity field is modelled as a uniform axial mean flow and an unsteady travelling wave moving along the axial direction at velocity $\overline{u}_c$ [35,36]

$$\boldsymbol{u} = \left(\overline{u}_1 + \epsilon \sin\left[\omega\left(t - x/\overline{u}_c\right)\right]\right)\boldsymbol{x}. \tag{12}$$

For small fluctuations amplitudes ϵ, the flame front can be considered a single-valued function of the radial coordinate, see Fig. 2. Within this limit, the *G*-equation can be linearized and solved, and the instantaneous heat release rate can be quantified by

$$Q = 2\pi \rho s_L h_r \iint_V |\nabla G| \delta(G) r \, dr \, dx. \tag{13}$$

Following steps analogous to those of [37,38], it can be shown that the FTF for the V-flame configuration outlined in Fig. 2 reads

$$\mathrm{FTF} = 2 \frac{e^{-\eta \mathrm{St}_2}\left(\gamma + \eta \mathrm{St}_2\right) - \eta e^{-\mathrm{St}_2}\left(\gamma + \mathrm{St}_2\right) + \gamma(\eta - 1)}{\eta \mathrm{St}_2^2(2 - \gamma)(1 - \eta)}. \tag{14}$$
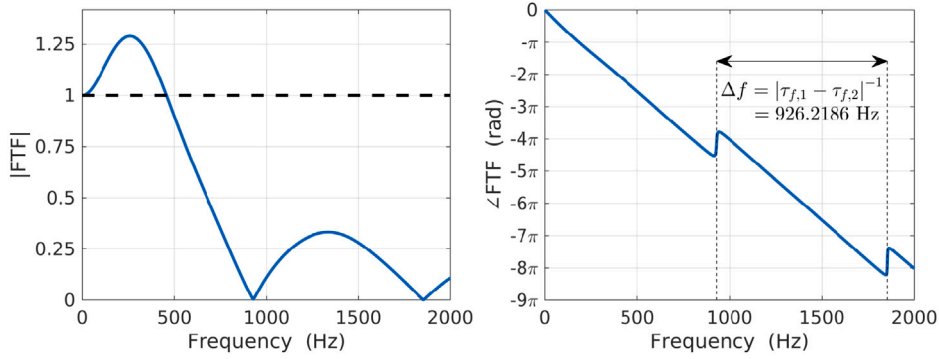
Fig. 3. Gain and phase of the V-flame FTF that will be used in this study. The non-dimensional parameters used are $\beta = 0.955$, $\gamma = 0.690$, $\eta = 0.645$. They are scaled by the cold mean flow velocity $\bar{u}_1 = 10$ m/s and the radial distance of the tip of the flame from the axis of symmetry, $R_w = 21$ mm.

In the latter, we have introduced the following non-dimensional variables:

$$\beta \equiv \frac{L_f}{R_w}, \qquad \gamma \equiv \frac{R_w - R_i}{R_w}, \qquad \sin\alpha = \frac{s_L}{\bar{u}_1} = \frac{R_w - R_i}{\sqrt{L_f^2 + (R_w - R_i)^2}} = \frac{\gamma}{\sqrt{\beta^2 + \gamma^2}}, \qquad \mathrm{St}_2 \equiv \frac{s L_f}{\bar{u}_1 \cos^2\alpha}, \qquad \eta \equiv \frac{\bar{u}_1}{\bar{u}_c}\cos^2\alpha. \tag{15}$$

This FTF is a generalization of that presented in Equation (28) of [37], in that the flame we consider is not (necessarily) anchored on the symmetry axis. The results of [37] are retrieved when setting $\gamma = 1$. The FTF that will be used in the rest of this study is shown in Fig. 3.

We note that the FTF (14) depends on two time scales, $\tau_{f,1} \equiv \mathrm{St}_2/s$ and $\tau_{f,2} \equiv \eta\mathrm{St}_2/s$. The first is the characteristic time that perturbations take to travel along the unperturbed flame extension, $L_f/\cos\alpha$, when carried by the component of the mean velocity parallel to the unperturbed flame, $\bar{u}_1\cos\alpha$. This time scale was recognized as a characteristic time scale in both conical and V-flames in [39,40]. The second time scale is the characteristic time taken by velocity disturbances to travel along the axial extension of the flame L_f at the convective velocity $\bar{u}_c$. As discussed in [37], it is the constructive (destructive) interference between the waves propagating with these characteristic times that causes the presence of maxima (minima) in the amplitude of the FTF. This is shown in Fig. 3, where the distance between two zeros in the FTF response has been calculated analytically from knowledge on the characteristic time scales.

3. Effective can reflection coefficient with experimental can-to-can impedance model

The work of [23] has identified semi-empirical models that characterize the impedance of a side-branch aperture. These models were fitted against the experimental data of [21] by using a standard least-square method. For the purpose of this manuscript, we shall adopt an impedance model based on the Rayleigh conductivity of an aperture with bias flow [41]

$$K_r(\Omega) = w\left[\frac{\pi}{2F(\Omega) + \log\frac{8w}{e l_g}} + \gamma_1\right]. \tag{16}$$

The non-dimensional function F is defined by[2]

$$F(\Omega) = \frac{-J_0 K - (J_0 + 2K)(J_0 + i\Omega(J_0 - iJ_1))}{\Omega(J_0 J_1 + \Omega(J_1^2 + (J_0 + 2iJ_1)^2))}, \tag{17}$$

where w is the transverse dimension of the aperture, $K \equiv i\Omega(J_0 + iJ_1)$, and $J_i = J_i(\Omega)$ are Bessel functions. The non-dimensional complex frequency used to evaluate the Rayleigh conductivity is $\Omega \equiv -is l_g/(2U_c)$, where $U_c \equiv \kappa\overline{U}$ is the characteristic convective velocity in the shear layer. From the definition of the Rayleigh conductivity, the impedance model for the aperture (9) is

$$\bar{\zeta} = \frac{s A_g}{K_r(\Omega)c} + \gamma_2. \tag{18}$$

The non-dimensional coefficients γ_1 and γ_2 in Eqs. (16) and (18) are introduced to account for radiation losses and three dimensional effects. Together with κ, they are fitted against the experimental results of [21]. Fig. 4 compares the measured and fitted resistance, $\Re[\zeta]$, and reactance, $\Im[\zeta]$, of the impedance at the connection cavities. Notably, there exists a frequency range within which the resistance becomes negative, which implies the generation of acoustic energy at that component [23]. This is a necessary but not sufficient condition for inducing an acoustic instability of the can-annular system that is driven by the aeroacoustics of the shear layers at the interfaces between the cans.

---

[2] Eq. (17) is the complex conjugate of the expression reported in Eq. (3.3) of [41]. The complex conjugation is needed to compensate the different conventions used in the definition of the Laplace variable.
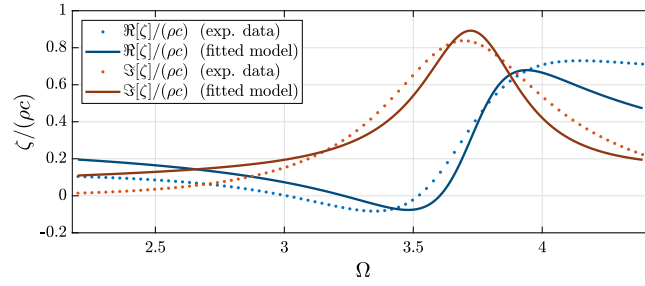
Fig. 4. Fit of the impedance model (18) against the frequency response of the shear layer reported in [21,23]. The fitted coefficient values are $\kappa = 0.412$, $\gamma_1 = -0.196 + 0.162i$ and $\gamma_2 = 0.154 + 0.079i$.
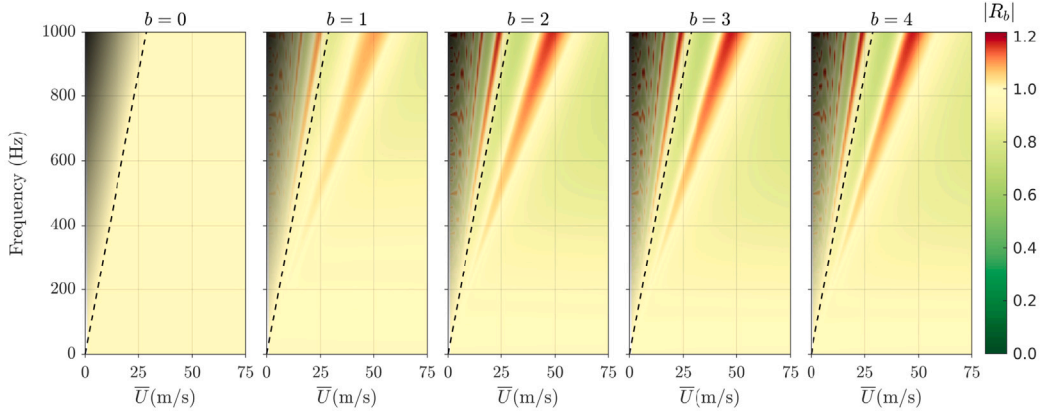

Fig. 5. Effective reflection coefficient magnitude for a system with $N = 8$ cans, as a function of the mean flow and the frequency. The dashed lines indicate the upper limit of the data of [21] to which the aperture impedance model (18) has been fitted. Above this line (shaded regions), the higher the frequency the less reliable the fitted model.

To demonstrate how Eq. (10) can be used to understand the effect that the can-to-can coupling has on the effective reflection coefficient, we set up a generic system with $N = 8$ cans, and use the can-to-can impedance model (18) to represent the interaction of the cans. The can impedance downstream of the aperture is chosen to be representative of the experimental configuration that will be considered in the following sections. It reads

$$\tilde{Z}_{ds} \equiv \frac{Z_{ds}}{\rho c} = \frac{e^{s\tau_{end}} - 1}{e^{s\tau_{end}} + 1}, \quad \text{with} \quad \tau_{end} = \frac{2l_{end}c}{c^2 - \overline{U}^2}, \tag{19}$$

which is the impedance of a tube of length l_{end} with mean flow and an open-end — when neglecting radiation and effective length corrections. Fig. 5 shows the magnitude of the effective reflection coefficients for all positive values of the Bloch number b as a function of the mean flow and frequency. For $b = 0$, the can-to-can connection has no influence on the reflection coefficient. The (small) deviations from $R = 1$ are due to variations in the grazing flow Mach number. For $b > 0$, the effective reflection coefficient is strongly influenced by the flow properties and the forcing frequency. For any value of the convective mean flow u_c, we can identify a frequency at which the magnitude of the effective reflection coefficient for a specific Bloch number is minimized, and a frequency at which it is maximized. Notably, the magnitude of the effective reflection coefficient can exceed 1, due to the fact that, at its resonance frequency, the aerodynamic shear layer acts as an amplifier and enhances small impinging perturbations, since the resistance takes negative values in this frequency range — see Fig. 4.

4. Thermoacoustic analysis of an atmospheric can-annular setup

The geometry we consider is an atmospheric can-annular setup, discussed in detail in [17]. It consists of 8 identical cans. Its geometrical details are reported in Fig. 6. In the experiment, the cans are mounted on a large plenum upstream, which could couple the acoustics also on that side. To avoid this coupling, a reflective sintered plate is mounted at the connection between the plenum and the tubes. This plate was characterized experimentally by means of the multi-microphone method in [18]. From the scattering matrix coefficients shown in Fig. A2 of the latter study, one can infer that for frequencies below 1.5 kHz, the reflection coefficient of the plate is about 0.8 (it coincides with the S_{11} element of their scattering matrix). We therefore set $R_1 = 0.8$ in Eq. (6).

The downstream boundary condition of the modelled portion of the can is the Bloch-number dependent reflection coefficient downstream of the aperture, Eq. (10). This requires a model for the response of the shear layer at the apertures and the downstream
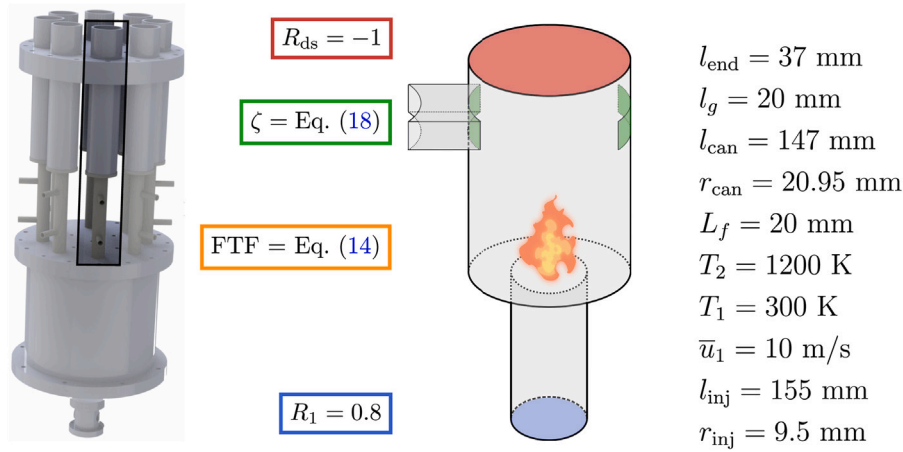
$$R_{ds} = -1$$

$$\zeta = \text{Eq. (18)}$$

$$\text{FTF} = \text{Eq. (14)}$$

$$R_1 = 0.8$$

$l_{end} = 37$ mm
$l_g = 20$ mm
$l_{can} = 147$ mm
$r_{can} = 20.95$ mm
$L_f = 20$ mm
$T_2 = 1200$ K
$T_1 = 300$ K
$\overline{u}_1 = 10$ m/s
$l_{inj} = 155$ mm
$r_{inj} = 9.5$ mm

Fig. 6. Left: rendering of the combustor considered in this study, with the Bloch-cell forming the highlighted can. Right: Sketch of the modelled can. The upstream boundary condition of the injectors (blue) is a reflective plate. A bluff-body stabilized flame is located at the intersection between the injector and the can. Close to the downstream end of the can, a small aperture (green) allows for the aeroacoustic communication with the adjacent cans. The downstream end of the can (red) is open. (For interpretation of the references to colour in this figure legend, the reader is referred to the web version of this article.)
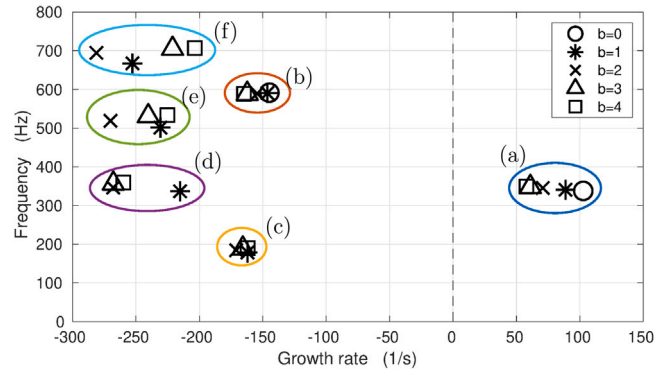

Fig. 7. Clusters of eigenvalues in the can-annular configuration considered. The markers differentiate the modes by their azimuthal phase pattern. The modes in clusters (a) and (b) are associated to eigenvalues of thermoacoustic origin. The clusters (c)–(f), instead, originate from the aeroacoustic coupling with the response of the shear layer in the apertures between two cans. Notably, these clusters lack the $b = 0$ mode since no dynamics in the apertures can occur if the cans oscillate in phase. (For interpretation of the references to colour in this figure legend, the reader is referred to the web version of this article.)

boundary condition just after the aperture in the scenario in which the apertures are closed. The former is given by Eq. (18), the latter by the impedance of an open-end tube of length $l_{end} = 37$ mm, Eq. (19). All geometrical, flow and thermal parameters, listed in Fig. 6, are chosen to be representative of the experiments described in [17]. The FTF is the only data that is not available from the experiments. It is therefore modelled by Eq. (14), using the geometrical/flow parameters of the experiment to determine the steady flame shape. The specific choice of the flame response is, however, not particularly important for the purpose of this study, which instead aims at providing a general modelling strategy for can-annular systems as lumped components. Furthermore, although the chosen G-equation based model may look simplistic, it captures all the general features of the linear response of premixed, laminar or turbulent V-flames, namely an amplifying frequency bend, a low-pass filtering characteristic, and an almost linear dependence of the phase on the frequency — see Fig. 3.

The spectrum of the semi-empirical can-annular combustor model described above (duct acoustics + FTF + Bloch boundary conditions + empirical can-to-can impedance) is shown in Fig. 7. The eigenvalues are obtained by using the integral method described in [42] to solve the nonlinear eigenvalue problem (6) for each value of the Bloch wavenumber b. The circular contour is centred at 500 Hz and has radius 490 Hz. Only the eigenvalues with frequencies below 800 Hz are discussed: above this frequency, the range of validity of the empirical can-to-can impedance is exceeded, and spurious modes may be found. The spectrum shown in Fig. 7 clearly exhibits the existence of clusters of eigenvalues. In particular, the clusters (a) and (b) can be related to frequencies which are close to the classic thermoacoustic frequencies of a single can. As will be further discussed in Section 4.1, cluster (a) is of acoustic origin whereas cluster (b) is of intrinsic origin [43,44]. Each of these clusters (a and b) comprises a total of 8 eigenvalues (counting multiplicity). In fact, due to the mirror symmetry of the Bloch cell, all eigenvalues found for Bloch numbers b in the range $0 < b < N/2$ are also eigenvalues of the system with Bloch number $-b$ [45]. For the $b = 0$ eigenvalues the effective reflection coefficient (10) reduces to the reflection coefficient of an open duct with mean flow. These eigenvalues are identical to those that
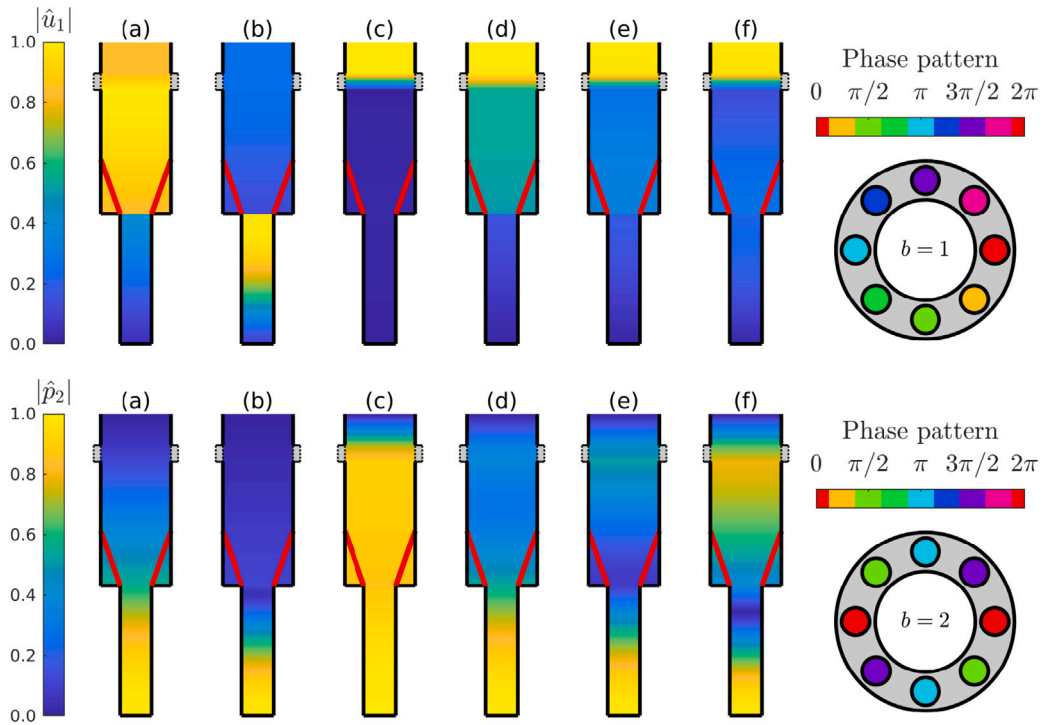
Fig. 8. Top: Acoustic velocity modeshapes $\hat{u}_b$ for Bloch number $b = 1$. Bottom: Acoustic pressure modeshapes $\hat{p}_b$ for Bloch number $b = 2$. With reference to Fig. 7, modeshapes (a) and (b) belong to clusters of thermoacoustic origin, whereas modeshapes (c) to (f) belong to clusters of aeroacoustic origin, in ascending frequency order. On the right end, a top view of the full annular combustor shows the phase oscillation patterns.

one would find if the connection orifices would be closed, and the dynamics in each can would be independent of that in the others. The clusters of eigenvalues (c) to (f) in Fig. 7, instead, are not originating from the can thermoacoustic response, but rather from the shear layer response in the apertures, and its interaction with the can acoustics. In fact, the lowest frequency (cluster (c), approx. 180 Hz) can be linked to the reciprocal of the time that a perturbation takes to travel along the aperture at the convective velocity $\bar{u}_c$; higher frequencies are multiples of this fundamental frequency. Notably, these clusters lack the $b = 0$ mode. This is correct because for $b = 0$, the cans oscillate in phase, and there is, hence, no dynamics in the apertures connecting the cans. These clusters therefore comprise only 7 eigenvalues (counting multiplicity; 3 semi-simple degenerate pairs for $b = \{1, 2, 3\}$ and a simple one for $b = 4$).

To gain further insight into the characteristics of the eigenvalues in the two types of clusters, Fig. 8 shows the acoustic velocity of the $b = 1$ eigenvalues and pressure modeshapes of the $b = 2$ eigenvalues. The acoustic field in the section of the can downstream of the aperture is reconstructed using planar propagation of acoustic waves in a duct with a mean flow. All modeshapes satisfy the upstream boundary condition (close to be a velocity node) and the open-end boundary condition at the downstream end of the can (pressure node). The pressure modes in the cluster of acoustic origin, (a), have the typical quarter-wave shape; the acoustic velocity has a discontinuity at the combustor inlet due the area change. The modeshapes of the modes in the cluster of intrinsic origin, (b), has a strong response in the injectors, with a maximum at the flame, consistently with the typical modeshapes of intrinsic origin [46]. Lastly, the modeshapes of the eigenvalues associated with the aperture dynamics, (c) to (f), have less canonical shapes. In particular, all the acoustic velocity modeshapes have a low intensity in the whole section upstream of the aperture, followed by a strong gradient across the aperture and a maximum in the can's downstream ends.

4.1. Eigenvalue cluster sensitivity

The identified eigenvalue clusters can be related to three fundamentally different physical mechanisms: acoustic, intrinsic and shear layer dynamics. It is therefore reasonable to expect that their sensitivity to variations in the system parameters will be different, and depend on the influence that a specific parameter has on the dynamics of the underlying physical mechanisms. In this section, we will systematically vary (i) the flame heat release response magnitude and (ii) the shear layer convective velocity, to investigate how these two parameters influence the evolution of the eigenvalue clusters.
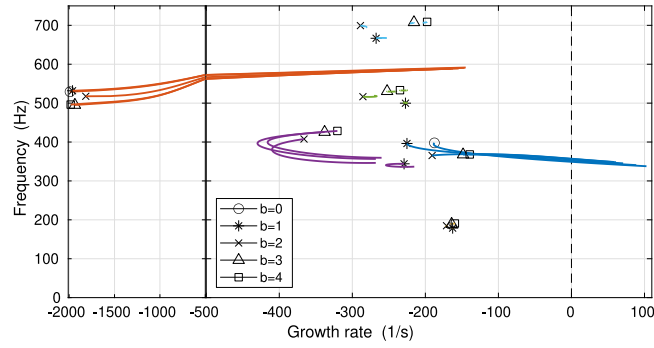
Fig. 9. Eigenvalue trajectories when the flame gain is decreased. The markers indicate the eigenvalues (by their Bloch-number) in the passive flame case, i.e., in the limit $|\text{FTF}_\xi| \to 0$. The colour-scheme corresponds to that used in Fig. 7 to emphasize the existence of clusters of eigenvalues. (For interpretation of the references to colour in this figure legend, the reader is referred to the web version of this article.)
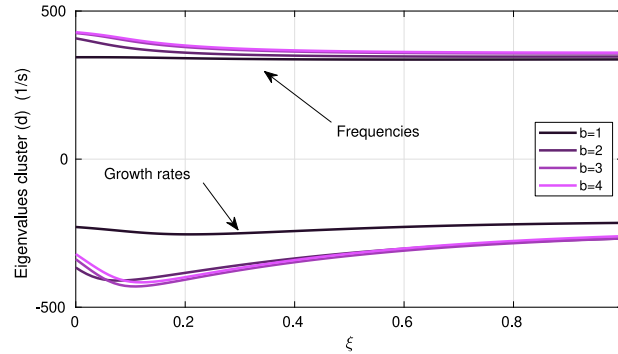

Fig. 10. Evolution of the eigenvalues of cluster (d) when ξ is varied in Eq. (20).

4.1.1. Sensitivity to FTF magnitude

To study the influence of the flame response strength on the eigenvalue clusters, we introduce a scaling parameter ξ in the definition of the FTF

$$\text{FTF}_\xi(s) = \xi\text{FTF}(s) \tag{20}$$

and we use this scaled Flame Transfer Function FTF_ξ in the definition of the heat release matrix response (5). When $\xi = 1$, the original FTF definition is unaffected, and the spectrum of the can-annular thermoacoustic system corresponds to that shown in Fig. 7. When $\xi = 0$, instead, the flame response vanishes – i.e., $\mathcal{M}_{\text{hr}} = \mathbf{0}$ in Eq. (5) – and only the aeroacoustic can-annular response in the absence of an active heat source is identified.

Fig. 9 shows the evolution of the eigenvalues in all clusters when ξ is varied in the range [0,1]. The colours identify the clusters, in accordance to Fig. 7, and the markers indicate the Bloch-number associated with each eigenvalue and are located in the $\xi \to 0$ limit. The cluster of acoustic origin (a) moves into the stable half-plane ($\sigma < 0$) when the flame is switched off; indeed, in the absence of an active flame source, no thermoacoustic instability can occur. The cluster of intrinsic origin (b) is pushed towards growth rates tending to $-\infty$ as $\xi \to 0$. It was shown in [44,47] that, in the vanishing flame limit, all the Bloch modes of this cluster tend towards the same frequency value, which can be predicted theoretically from the coefficients of the scattering matrix at the flame (see Appendix of [44]).

The remaining clusters, (c) to (f), are of shear layer dynamics origin. Their physical nature is not closely connected to the heat release dynamics, and it is reasonable to expect them to be almost independent of the flame response. This is true for clusters (c), (e) and (f), but not for cluster (d). The sensitivity of cluster (d) to the flame dynamics can be attributed to the fact that, when the flame dynamics is turned off ($\xi = 0$), its eigenvalues have both frequencies and growth rates close to those of cluster (a). This suggests that close-by in parameter space the eigenvalues coalesce, becoming degenerate. As discussed in [48], eigenvalues that are close to being degenerate exhibit a phenomenon known as mode veering. To avoid crossing, the eigenvalues steer away from each other. This can be observed in Fig. 9, which shows that the trajectories of the (a) and (d) clusters move in opposite directions for small values of ξ – close to the markers. To emphasize this further, Fig. 10 shows the dependence of the eigenvalues in cluster (d) on the parameter ξ. The sensitivity of the eigenvalues (slope of the curves) is non-uniform and high for small values of ξ, but tends to flatten as ξ becomes larger. When the eigenvalues of clusters (d) are sufficiently far from those of cluster (a), the sensitivity of the eigenvalues of cluster (d) to the intensity of the flame becomes very small, similar to those of clusters (c), (e) and (f).
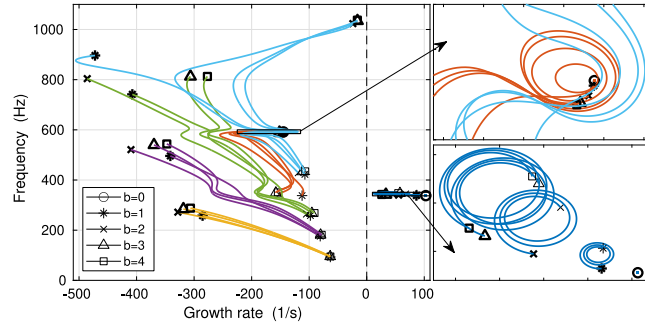
Fig. 11. Eigenvalue trajectories when the convective speed in the aperture between cans is varied. Thick and thin markers indicate, respectively, the eigenvalues (by their Bloch-number) for the maximum (thick markers, $\kappa = 0.62$) and minimum (thin markers, $\kappa = 0.2$) convective speed considered. The colour-scheme corresponds to that used in Fig. 7 to emphasize the existence of clusters of eigenvalues. Right panels: magnification of the regions highlighted. (For interpretation of the references to colour in this figure legend, the reader is referred to the web version of this article.)

4.1.2. Sensitivity to aeroacoustic coupling

We shall now focus on the sensitivity that the shear layer response has on the can-annular system's spectrum. In particular, we will investigate the effect of the convective speed in the shear layer, $U_c \equiv \kappa \overline{U}$, by varying the non-dimensional value κ in the range [0.2,0.62]. The mean flow velocities in the cold/hot regions of the can-annular system are unchanged. The trajectories of the eigenvalue clusters obtained while varying κ are shown in Fig. 11. The thin (thick) markers identify the eigenvalues obtained for the minimum (maximum) values of κ considered.

First, we note that the $b = 0$ eigenvalues are not affected by κ. This is because only the can-to-can impedance (18) is affected by this parameter. For $b = 0$ the cans oscillate in phase, so that the pressure drop between neighbouring cans vanishes, and the can-to-can impedance does not play any role. The eigenvalues of the cluster of acoustic origin (a) are almost unaffected by this parameter, as emphasized in the bottom-right inset of Fig. 11. Its eigenvalues with $b \neq 0$ exhibit loop patterns. This cyclic behaviour is a manifestation of the phase induced by the convective time scale in the shear layer, which scales with l_g/U_c. It is analogous to the eigenvalue behaviour described in [49] when varying the time delay of the heat release response. Cluster (b), of intrinsic origin, has a non-trivial response to variations in the convective velocity. For small values of κ, its frequency is particularly sensitive to variations in the shear layer convective speed. For larger values of κ, a cyclic behaviour is again observed, emphasized in the top-right inset of Fig. 11.

Clusters (c) to (f) are the most sensitive to a variations of κ, since they are directly related to the shear layer dynamics. Since the shear layer convection speed enters in the definition of the non-dimensional frequency Ω in the Rayleigh conductivity (16), increasing (decreasing) κ shifts the peak of the response of the can-to-can impedance (Fig. 4) towards higher (lower) frequencies. The convection speed also has a significant effect on the growth rates of the eigenvalues of these clusters. For almost all the eigenvalues in these clusters, the larger the convection speed, the more stable are the eigenvalues. Additionally, for smaller values of κ the eigenvalue clusters are more dense, in the sense that a cluster is confined in a smaller portion of the complex frequency space.

5. Acoustically closed downstream end

A major difference between the experimental setup of [17] modelled in Section 4 and can-annular combustors in gas turbines is that in the former the cans are acoustically open at the downstream end, whereas in the latter the flow is nearly choked at the connection between the cans and the turbine inlet. Since the apertures that connect the cans are close to the downstream ends, they are located close to an acoustic pressure node when the cans are acoustically open. In this scenario, the coupling between the aerodynamics of the shear layer in the apertures and the thermoacoustics of the can is generally weaker, since it depends on the pressure difference between the cans [25,34], which remains small close to a pressure node. This was already visible in Fig. 9, in which almost all eigenvalues of aeroacoustic origin had very negative growth rates, corresponding to the (stable) dynamics of the decoupled aeroacoustic modes. On the contrary, for an acoustically closed boundary condition, which is a reasonable approximation for a choked end [19], the apertures are located in the vicinity of a pressure antinode. In this scenario, the pressure differences between neighbouring cans can be significantly higher, enhancing the can-to-can communication effects. In this last section, we will discuss how the spectrum and mode shapes of the can-annular system vary when the downstream boundary condition is acoustically closed.

An acoustically closed end of the cans, downstream of the aperture, can be modelled by setting the downstream impedance to $Z_{ds} = \infty$ in place of Eq. (19). In this limit, the effective downstream reflection coefficient (10) simplifies to

$$R_b = 1 - 2 \frac{4 A_r/\tilde{\zeta} \sin^2\left(\frac{\pi b}{N}\right)}{\left(1 - M_x^2\right) + 4 A_r/\tilde{\zeta} \sin^2\left(\frac{\pi b}{N}\right)}. \tag{21}$$

Except for the downstream boundary condition, all the other parameters are kept to those presented in Section 4.
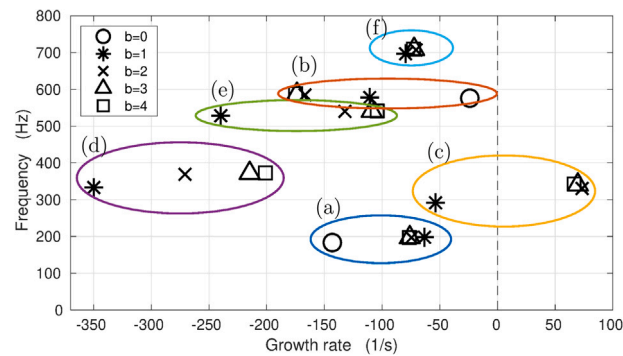
Fig. 12. Clusters of eigenvalues in the can-annular configuration considered with a closed end. The markers differentiate the modes by their azimuthal phase pattern. The modes in clusters (a) and (b) are associated with eigenvalues of thermoacoustic origin. The clusters (c)–(f), that lack the $b = 0$ mode, originate from the aeroacoustic coupling with the response of the shear layer in the apertures between two cans. Notably, it is a cluster of aeroacoustic origin that becomes unstable.

Fig. 12 shows the spectrum of the can-annular system with a closed boundary condition. The existence of eigenvalue clusters has been emphasized, and the eigenvalues are distinguished by their Bloch-number, following the same colour and marker conventions of Fig. 7. Clusters (a) and (b) are clusters of classic thermoacoustic origin. We note how the frequencies and growth rates of cluster (a), which is of acoustic origin, have significantly changed compared to those of the open-end configuration, since acoustic modes are strongly affected by the boundary conditions. On the other hand, the frequencies of cluster (b) are very similar to those found for an open end. This is consistent with the fact that this cluster was found to be associated with an intrinsic mode, and it is mostly ruled by the flame dynamics – unchanged with respect to the results shown in Fig. 7 – and not by the acoustics. Clusters (c) to (f) of Fig. 12 are associated with modes of aeroacoustic origin, as can be seen by the fact that they lack the $b = 0$ eigenvalues. The stronger coupling between the aeroacoustics of the apertures and the thermoacoustics of the cans in comparison to the open-end case can be seen by the fact that the growth rates of these eigenvalues are significantly different, and tend to have larger values. In particular, some of the eigenvalues of cluster (c) now have positive growth rates, implying that an instability in this configuration will mostly be driven by the aeroacoustics in the apertures.

The mode shapes associated with some of the eigenvalues of Fig. 12 are shown in Fig. 13. In comparison to Fig. 8, the downstream open tube is missing since it has been replaced by a sound-hard end. Thus, the mode shapes exhibit qualitative differences as the acoustic pressure needs to now exhibit a pressure antinode at the downstream end rather than a node, and vice versa for the acoustic velocity. An exception to this observation occurs for cluster (b), the cluster associated with an intrinsic mode, which is therefore relatively insensitive to variations in the boundary conditions [44]. For this reason, both the pressure and acoustic mode shapes of cluster (b) are similar for open (Fig. 8) or closed (Fig. 13) boundary conditions. It is interesting to note how in clusters (c) to (f) the magnitude of the acoustic pressure field remains not very high close to the downstream end, despite having a local maximum close to the apertures, and has instead large pressure amplitudes upstream of the flame. By looking at the mode shapes only, it would therefore be difficult to determine the origin of these modes.

6. Conclusions

In this study, we have presented a general reduced-order model for investigating the thermoacoustic properties of can-annular combustors. Particular focus was placed on appropriately modelling the can-to-can communication, which was accomplished by embedding in the model semi-empirical impedance expressions fitted against experimental data. The modelling approach exploits Bloch-wave theory and reduces the analysis to a single can, equipped with an effective boundary condition that contains the aeroacoustic response of the apertures and the acoustic properties of the can downstream of the aperture.

The model was used to study the response of an existing atmospheric can-annular test-rig. Since the flame response data is not available, the flame dynamics has been approximated by that of a V-flame, modelled with the kinematic G-equation. The spectrum of the setup has been determined, highlighting the presence of clusters of eigenvalues. The origin of the clusters has been discussed, emphasizing how some clusters originate from the aeroacoustic response of the aperture, and not the acoustic response of the can. These clusters are peculiar in that they lack the presence of $b = 0$ (in-phase oscillation) modes. They, therefore, cannot be predicted if the can-to-can communication is ignored.

The properties of eigenvalues and eigenvectors having different physical origins – related to the acoustic, intrinsic and shear layer dynamics, respectively – have been discussed. In particular, a parametric analysis has been performed to demonstrate that the sensitivity of the eigenvalues with respect to specific parameters is strongly dependent on their physical origin. Lastly, the effect of the downstream boundary conditions has been analysed and discussed, emphasizing the differences between the can-to-can coupling in atmospheric experiments – whose downstream boundary condition can be approximated by an acoustically open end – and real gas turbine combustors – whose downstream boundary condition can be approximated by an acoustically closed end. Our discussion highlights how knowledge on the physical mechanisms that are responsible for the creation of a particular eigenvalue
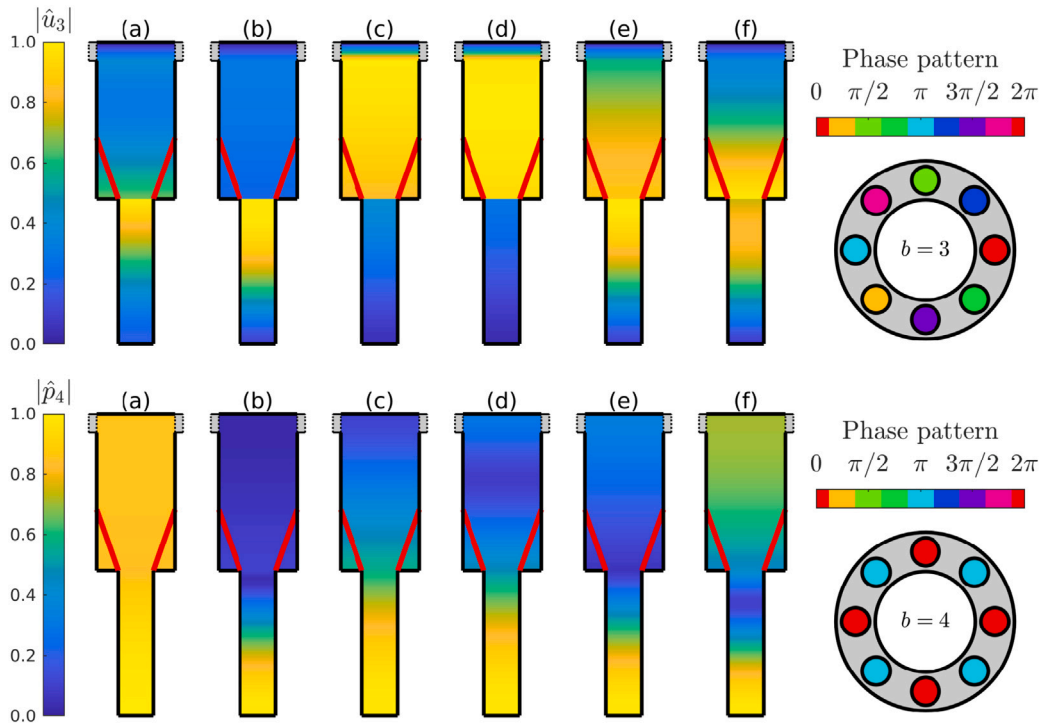
Fig. 13. Modeshapes for the $Z_{ds} = \infty$. Top: Acoustic velocity modeshapes $\hat{u}_b$ for Bloch number $b = 3$. Bottom: Acoustic pressure modeshapes $\hat{p}_b$ for Bloch number $b = 4$. With reference to Fig. 7, modeshapes (a) and (b) belong to clusters of thermoacoustic origin, whereas modeshapes (c) to (f) belong to clusters of aeroacoustic origin, in ascending frequency order. On the right end, a top view of the full annular combustor shows the phase oscillation patterns.

cluster is important for an assessment of the thermoacoustic spectrum, the eigenvalue sensitivities and their potential control. Future research on this topic will include the modelling of the nonlinear response of the apertures' dynamics, which, as recently shown by [21], may be non-negligible.

CRediT authorship contribution statement

Alessandro Orchini: Conceptualization, Methodology, Software, Visualization, Writing – original draft. **Tiemo Pedergnana:** Conceptualization, Methodology, Software, Resources, Writing – original draft. **Philip E. Buschmann:** Methodology, Software, Visualization, Resources. **Jonas P. Moeck:** Conceptualization, Methodology, Supervision, Writing – review & editing. **Nicolas Noiray:** Conceptualization, Methodology, Supervision, Writing – review & editing.

Declaration of competing interest

The authors declare that they have no known competing financial interests or personal relationships that could have appeared to influence the work reported in this paper.

Acknowledgements

References

[1] J.W.S. Rayleigh, The explanation of certain acoustical phenomena, Nature 18 (455) (1878) 319–321.
[2] J. Keller, Thermoacoustic oscillations in combustion chambers of gas turbines, AIAA J. 33 (12) (1995) 2280–2287.
[3] L. Crocco, Aspects of combustion stability in liquid propellant rocket motors part I: Fundamentals. Low frequency instability with monopropellants, J. Am. Rocket Soc. 21 (6) (1951) 163–178.
[4] J. Keller, W. Egli, J. Hellat, Thermally induced low-frequency oscillations, Z. Angew. Math. Phys. 36 (2) (1985) 250–274.
[5] T. Schuller, T. Poinsot, S. Candel, Dynamics and control of premixed combustion systems based on flame transfer and describing functions, J. Fluid Mech. 894 (2020).

[6] N. Noiray, B. Schuermans, On the dynamic nature of azimuthal thermoacoustic modes in annular gas turbine combustion chambers, Proc. R. Soc. Lond. Ser. A Math. Phys. Eng. Sci. 469 (2151) (2013).

[7] G. Ghirardo, M. Juniper, Azimuthal instabilities in annular combustors: Standing and spinning modes, Proc. R. Soc. Lond. Ser. A Math. Phys. Eng. Sci. 469 (2157) (2013) 20130232 (15 pages).

[8] S. Bethke, W. Krebs, P. Flohr, B. Prade, Thermoacoustic properties of can annular combustors, in: 8th AIAA/CEAS Aeroacoustics Conference And Exhibit, 2002, pp. 1–11.

[9] W. Krebs, S. Bethke, J. Lepers, P. Flohr, B. Prade, C. Johnson, S. Sattinger, Thermoacoustic design tools and passive control: Siemens power generation approaches, in: Combustion Instabilities In Gas Turbine Engines: Operational Experience, Fundamental Mechanisms, And Modeling, AIAA, 2005, pp. 89–112.

[10] P. Kaufmann, W. Krebs, R. Valdes, U. Wever, 3D thermoacoustic properties of single can and multi can combustor configurations, in: Proceedings Of The ASME Turbo Expo, 3A, 2008, pp. 527–538.

[11] F. Farisco, L. Panek, J.B.W. Kok, Thermo-acoustic cross-talk between cans in a can-annular combustor, Int. J. Spray Combust. 9 (4) (2017) 452–469.

[12] K. Venkatesan, A. Cross, C. Yoon, F. Han, S. Bethke, Heavy duty gas turbine combustion dynamics study using a two-can combustion system, in: Proceedings Of The ASME Turbo Expo, 4A, 2019, pp. 1–9.

[13] K. Moon, H. Jegal, C. Yoon, K.T. Kim, Cross-talk-interaction-induced combustion instabilities in a can-annular lean-premixed combustor configuration, Combust. Flame 220 (2020) 178–188.

[14] K. Moon, C. Yoon, K.T. Kim, Influence of rotational asymmetry on thermoacoustic instabilities in a can-annular lean-premixed combustor, Combust. Flame 223 (2021) 295–306.

[15] G. Ghirardo, C.D. Giovine, J.P. Moeck, M.R. Bothien, Thermoacoustics of can-annular combustors, J. Eng. Gas Turb. Power 141 (1) (2019) 011007 (10 pages).

[16] G. Ghirardo, J.P. Moeck, M.R. Bothien, Effect of noise and nonlinearities on thermoacoustics of can-annular combustors, J. Eng. Gas Turb. Power 142 (4) (2020) 041005 (10 pages).

[17] P.E. Buschmann, N.A. Worth, J.P. Moeck, Experimental study of thermoacoustic modes in a can-annular model combustor, in: SoTiC 2021 - Symposium On Thermoacoustics In Combustion: Industry Meets Academia, 2021.

[18] T. Indlekofer, B. Ahn, Y.H. Kwah, S. Wiseman, M. Mazur, J.R. Dawson, N.A. Worth, The effect of hydrogen addition on the amplitude and harmonic response of azimuthal instabilities in a pressurized annular combustor, Combust. Flame 228 (2021) 375–387.

[19] N. Lamarque, T. Poinsot, Boundary conditions for acoustic eigenmode computations in gas turbine combustion chambers, AIAA J. 46 (9) (2008) 2282–2292.

[20] C. Sondhauss, Ueber die beim Ausströmen der Luft entstehenden Töne   [On the sound generated by discharging air], Ann. Phys. (Leipzig) 167 (2) (1854) 214–240.

[21] C. Bourquard, A. Faure-Beaulieu, N. Noiray, Whistling of deep cavities subject to turbulent grazing flow: intermittently unstable aeroacoustic feedback, J. Fluid Mech. 909 (2021) A19.

[22] E. Boujo, M. Bauerheim, N. Noiray, Saturation of a turbulent mixing layer over a cavity: response to harmonic forcing around mean flows, J. Fluid Mech. 853 (2018) 386–418.

[23] T. Pedergnana, C. Bourquard, A. Faure-Beaulieu, N. Noiray, Modeling the nonlinear aeroacoustic response of a harmonically forced side branch aperture under turbulent grazing flow, Phys. Rev. Fluids 6 (2021) 023903.

[24] L. Panek, F. Farisco, M. Huth, Thermo-acoustic characterization of can–can interaction of a can-annular combustion system based on unsteady CFD LES simulation, in: Global Power And Propulsion Forum, 2017, GPPF–81 (5 pages).

[25] J. von Saldern, A. Orchini, J. Moeck, Analysis of thermoacoustic modes in can-annular combustors using effective Bloch-type boundary conditions, J. Eng. Gas Turbines Power 143 (7) (2021) 071019 (8 pages).

[26] S.W. Rienstra, A. Hirschberg, An Introduction to Acoustics, December, Eindhoven University of Technology, 2004.

[27] A.P. Dowling, Nonlinear self-excited oscillations of a ducted flame, J. Fluid Mech. 346 (1997) 271–290.

[28] A. Orchini, S.J. Illingworth, M.P. Juniper, Frequency domain and time domain analysis of thermoacoustic oscillations with wave-based acoustics, J. Fluid Mech. 775 (2015) 387–414.

[29] A. Orchini, Modelling and analysis of nonlinear thermoacoustic systems using frequency and time domain methods (Ph.D. thesis), University of Cambridge, 2016, p. 222.

[30] V. Bellucci, B. Schuermans, D. Nowak, P. Flohr, C.O. Paschereit, Thermoacoustic modeling of a gas turbine combustor equipped with acoustic dampers, J. Turbomach. 127 (2005) 372–379.

[31] F. Bloch, Über die Quantenmechanik der Elektronen in Kristallgittern [On the quantum mechanics of electrons in crystal lattices], Z. Phys. 52 (1929) 555–600.

[32] G.A. Mensah, G. Campa, J.P. Moeck, Efficient computation of thermoacoustic modes in industrial annular combustion chambers based on Bloch-wave theory, J. Eng. Gas Turbines Power 138 (2016) 081502 (7 pages).

[33] J.G.R. von Saldern, A. Orchini, J.P. Moeck, A non-compact effective impedance model for can-to-can acoustic communication: Analysis and optimization of damping mechanisms, J. Eng. Gas Turbines Power 143 (12) (2021) 121024 (10 pages).

[34] A. Orchini, An effective impedance for modelling the aeroacoustic coupling of ducts connected via apertures, J. Sound Vib. 520 (2022) 116622.

[35] A.L. Birbaud, D. Durox, S. Candel, Upstream flow dynamics of a laminar premixed conical flame submitted to acoustic modulations, Combust. Flame 146 (2006) 541–552.

[36] N. Karimi, M.J. Brear, S.-H. Jin, J.P. Monty, Linear and non-linear forced response of a conical, ducted, laminar premixed flame, Combust. Flame 156 (2009) 2201–2212.

[37] Preetham, S. Hemchandra, T. Lieuwen, Dynamics of laminar premixed flames forced by harmonic velocity disturbances, J. Propuls. Power 24 (6) (2008) 1390–1402.

[38] A. Orchini, M.P. Juniper, Linear stability and adjoint sensitivity analysis of thermoacoustic networks with premixed flames, Combust. Flame 165 (2016) 97–108.

[39] T. Schuller, D. Durox, S. Candel, A unified model for the prediction of laminar flame transfer functions: comparisons between conical and V-flames dynamics, Combust. Flame 134 (2003) 21–34.

[40] R.S. Blumenthal, P. Subramanian, R. Sujith, W. Polifke, Novel perspectives on the dynamics of premixed flames, Combust. Flame 160 (7) (2013) 1215–1224.

[41] M. Howe, Influence of wall thickness on rayleigh conductivity and flow-induced aperture tones, J. Fluids Struct. 11 (4) (1997) 351–366.

[42] P.E. Buschmann, G.A. Mensah, F. Nicoud, J. Moeck, Solution of thermoacoustic eigenvalue problems with a non-iterative method, J. Eng. Gas Turbines Power 142 (3) (2020) 031022 (11 pages).

[43] T. Emmert, S. Bomberg, W. Polifke, Intrinsic thermoacoustic instability of premixed flames, Combust. Flame 162 (2015) 75–85.

[44] A. Orchini, C.F. Silva, G.A. Mensah, J.P. Moeck, Thermoacoustic modes of intrinsic and acoustic origin and their interplay with exceptional points, Combust. Flame 211 (2020) 83–95.

[45] G.A. Mensah, L. Magri, A. Orchini, J.P. Moeck, Effects of asymmetry on thermoacoustic modes in annular combustors: A higher- order perturbation study, J. Eng. Gas Turb. Power 141 (2019) 041030 (8 pages).

[46] E. Courtine, L. Selle, T. Poinsot, DNS Of intrinsic thermoacoustic modes in laminar premixed flames, Combust. Flame 162 (2015) 4331–4341.

[47] P.E. Buschmann, G.A. Mensah, J.P. Moeck, Intrinsic thermoacoustic modes in an annular combustion chamber, Combust. Flame 214 (2020) 251–262.

[48] A. Orchini, L. Magri, C. Silva, G. Mensah, J. Moeck, Degenerate perturbation theory in thermoacoustics: High-order sensitivities and exceptional points, J. Fluid Mech. 903 (2020) A37 (30 pages).

[49] C.F. Silva, W. Polifke, Non-dimensional groups for similarity analysis of thermoacoustic instabilities, Proc. Combust. Inst. 37 (2019) 5289–5297.